

Direction-Dependent Conduction Polarity in Altermagnetic CrSb

Banik Rai^{1,3}, Krishnendu Patra^{1,3}, Satyabrata Bera², Kakan Deb¹, Mintu Mondal², Priya Mahadevan^{1,*}, and Nitesh Kumar^{1,**}

¹Department of Condensed Matter and Materials Physics, S. N. Bose National Centre for Basic Sciences, Salt Lake City, Kolkata-700106, India

²School of Physical Sciences, Indian Association for the Cultivation of Science, Jadavpur, Kolkata-700032, India

³These authors contributed equally to this work.

*Contact author: priya@bose.res.in

**Contact author: nitesh.kumar@bose.res.in

CrSb has recently gained immense attention as an altermagnetic candidate. This work reports on the experimental observation of direction-dependent conduction polarity (DDCP) in altermagnetic CrSb through Hall and Seebeck thermopower measurements. Conduction is dominated by holes along the *c*-axis and by electrons in the *ab*-plane of the hexagonal crystal of CrSb. Density functional theory (DFT) calculations indicate that DDCP in CrSb arises from a multi-carrier mechanism, where electrons and holes living in distinct bands dominate conduction along different crystallographic directions. Furthermore, DFT predicts that DDCP exists within a narrow energy window near the Fermi level and is sensitive to small doping levels. This prediction is experimentally validated by the loss of DDCP in hole-doped Cr_{0.98}V_{0.02}Sb. These findings highlight the potential for tunable electronic behavior in CrSb, offering promising avenues for applications in devices that require both p-type and n-type functionalities within a single material.

1 Introduction

Almost all materials (metals and semiconductors) have a single type of dominant charge carrier, either electrons or holes, along all crystallographic directions. This allows these materials to be easily classified as either n-type (electron dominant) or p-type (hole dominant). However, there exists a rare and distinct class of materials that defies this simple classification. [1–7] These unique materials can exhibit electron- and hole-dominant conduction simultaneously along different crystallographic directions. This direction-dependent conduction polarity (DDCP), is enabled by the geometrical features of the Fermi surface (FS). The effective mass tensor of a charge carrier moving through a crystal lattice potential is given by:

$$m_{ij}^* = \hbar^2 \left[\frac{\partial^2 E}{\partial k_i \partial k_j} \right]_{E=E_F}^{-1}. \quad (1)$$

Electrons have positive m_{ij}^* while holes have negative m_{ij}^* . Since the second derivative of a function determines its curvature, m_{ij}^* can be positive or negative depending on the curvature of the corresponding energy band crossing the Fermi energy (E_F). DDCP can be realized if the integrated curvature of all the bands crossing E_F is positive in one direction and negative in the other. The FS, which provides a geometric representation of all points in reciprocal space where the band energy equals E_F , encompasses all bands crossing E_F . A single band material can exhibit DDCP if its FS has concave and convex characters along different directions [see Figure 1a]. This has been observed in NaSn₂As₂, [1] which has a hyperboloid-shaped FS that has both positive and negative curvatures (dependent on direction). The DDCP arising from single carrier mechanism is termed “goniopolarity”, and the materials exhibiting it are called “goniopolar”. Another way to achieve DDCP is through multicarrier mechanism [see Figure 1(b-c)], where electrons and holes live in two distinct bands and dominate conduction along different crystallographic directions. [2,6] This can be achieved when the FS exhibits highly anisotropic electron and hole pockets, such that the integrated curvature of the total FS has opposite signs along two different crystallographic directions.

Although materials exhibiting DDCP have recently gained attention as novel thermoelectric materials, [8–10] only a handful of such materials have been discovered to date. Among these, very few are both air-stable and composed of earth-abundant elements, which are essential prerequisites for practical device applications and commercialization. Additionally, inconsistencies often arise in the experimental characterization of reported DDCP materials. For example, the Hall coefficient and Seebeck coefficient, whose signs are key indicators of DDCP, may exhibit conflicting signs [1] or one of them fail to demonstrate the direction-dependent opposite signs, [9] which is the defining feature of DDCP.

In this paper, we investigate the transport properties of the recently identified altermagnetic candidate CrSb. Altermagnets represent a novel phase of collinear magnets with vanishing magnetization and spin-split energy bands, [11,12] making them an important material for

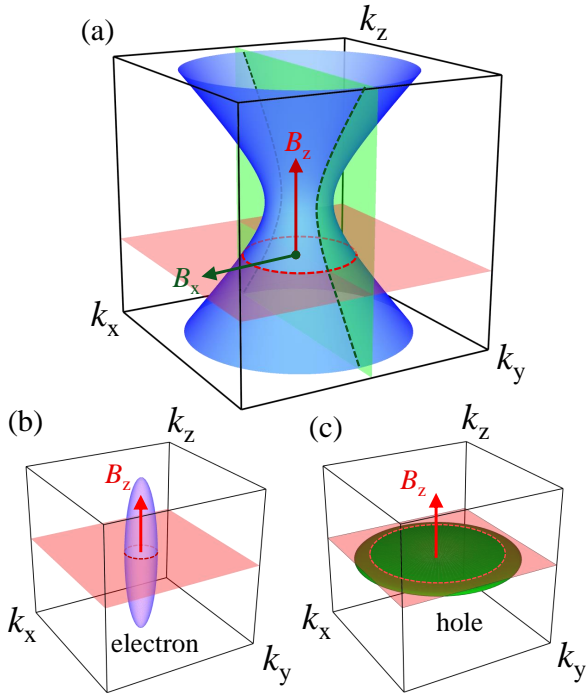


Figure 1. FS geometries for DDCP via single carrier and multicarrier mechanisms. (a) Hyperboloid FS for single carrier mechanism exhibiting convex character in the $k_x - k_y$ plane and concave character along the k_z direction, with dashed lines representing the possible charge carrier trajectories for different magnetic field directions. (b)-(c) Anisotropic Fermi pockets for the multicarrier mechanism, where, without loss of generality, the left pocket represents an electron pocket and the right pocket represents a hole pocket. The electron pocket is elongated along the k_z direction, while the hole pocket is flat in the $k_x - k_y$ plane. A possible electron and hole trajectory is shown with dashed lines for a magnetic field applied along the z -direction. Electrons dominate conduction in the $k_x - k_y$ plane, while the holes dominate conduction along k_z -direction.

future spintronics applications. We report the observation of DDCP in CrSb, based on Hall and thermopower measurements. Both the Hall coefficient and Seebeck coefficient indicate that the conduction is dominated by holes along the c -axis and by electrons in the ab -plane of the CrSb hexagonal crystal. This behavior is qualitatively supported by our DFT calculations. The FS calculated by DFT consists of two hole pockets and one electron pocket. The DDCP in CrSb emerges as the electron and hole pockets dominate conduction along different crystallographic directions. DFT also predicts that the DDCP is confined in a narrow energy window ($\Delta E \approx 14$ meV) near E_F and can be suppressed by doping. This prediction is experimentally validated, as a doping of ~ 0.04 number of holes per unit cell in $\text{Cr}_{0.98}\text{V}_{0.02}\text{Sb}$ destroys the DDCP and drives the system towards p-type.

Given that both Cr and Sb are earth-abundant and relatively non-toxic elements, CrSb holds great promise for practical applications that exploit its DDCP behavior. Furthermore, its altermagnetic properties introduce

an intriguing aspect, paving the way for future spintronics applications that leverage both DDCP and spin-splitting phenomena.

2 Results and Discussion

CrSb crystallizes in a hexagonal NiAs-type structure with space group $P6_3/mmc$ and exhibits A-type antiferromagnetic order with a Néel temperature of approximately 703 K. [13,14] The Cr moments are aligned parallel to the c -axis, coupled ferromagnetically in the ab -plane and antiferromagnetically along the c -axis [see Figure 2a]. The anisotropic arrangement of Sb atoms around the oppositely aligned Cr spins prevents the connection of opposite spin sublattices by simple lattice translations or inversion [see Figure 2b]. However, these sublattices can be connected either by a six-fold crystal rotation about the c -axis (C_{6z}) combined with half the lattice translation along the c -axis ($t_{1/2} = (0, 0, c/2)$) or by a horizontal mirror (M_z) passing through the Sb layer. These operations, when combined with time-reversal symmetry (τ), yield the actual sublattice-transposing symmetries of the crystal: $C_{6z}t_{1/2}\tau$ and $M_z\tau$. These symmetries give rise to four spin-degenerate nodal planes in the Brillouin zone (BZ) (see Supporting Information). Away from these high-symmetry nodal planes, the spin degeneracy is lifted, resulting in significant non-relativistic splitting of the energy bands (see Supporting Information).

To examine the transport behavior of CrSb along different crystallographic directions, the coordinate axes have been defined on the hexagonal lattice of CrSb [see Figure 3a]. The x - and z -axes align with the crystallographic a - and c -directions whereas the y -axis is along the crystallographic $[01\bar{1}0]$ direction. Figure 3b shows the temperature dependence of in-plane (ρ_{yy}) and cross-plane (ρ_{zz}) longitudinal resistivity. The material shows metallic nature throughout the temperature range in both in-plane and cross-plane directions with almost coinciding resistivity values and similar residual resistivity ratios ($RRR \approx 3.7$). The field dependent Hall resistivity

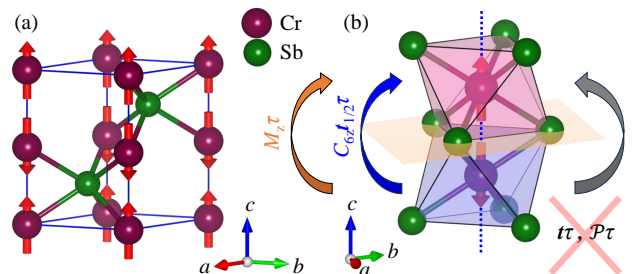


Figure 2. Crystal structure and sublattice transposing symmetries of CrSb. (a) Magnetic unit cell of CrSb showing A-type antiferromagnetic ordering of Cr moments. (b) Sublattice transposing symmetries of CrSb showing that a lattice translation or inversion does not connect the opposite spin sublattices, which are instead connected by a horizontal mirror passing through Sb layer or a real space crystal rotation combined with half the lattice translation along the c -axis.

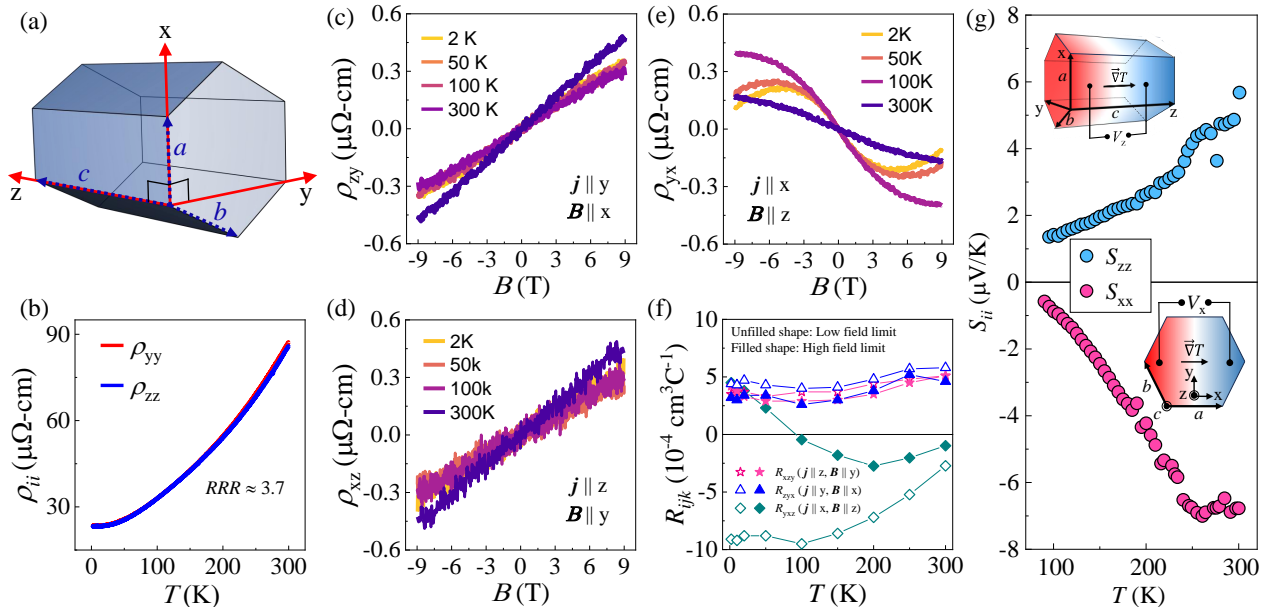


Figure 3. Electrical transport properties and Seebeck effect in CrSb. (a) Defining coordinate axes on the hexagonal unit cell of CrSb. (b) In-plane (ρ_{yy}) and cross-plane (ρ_{zz}) longitudinal resistivity as a function of temperature. (c)-(e) Magnetic field dependent Hall resistivity for different Hall geometries. (f) Variation of Hall coefficient as a function of temperature for different Hall geometries. (g) In plane (S_{xx}) and cross-plane (S_{zz}) Seebeck coefficients as a function of temperature.

data in different geometries are shown in Figure 3(c-e). When a magnetic field is applied within the hexagonal plane of the CrSb crystal, as illustrated in Figure 3c and 3d for $B||x$ and $B||y$ respectively, both the Hall resistivity ρ_{zy} and ρ_{xz} exhibit an almost linear dependence on the field at all temperatures with similar positive slopes. When the magnetic field is applied along the z-axis, the Hall resistivity ρ_{yx} deviates from linearity, especially at lower temperatures, and the slopes becomes predominantly negative. This non-linear behavior in Hall resistivity is often associated with the anomalous Hall effect [15] or a multicarrier transport mechanism. [16] Since the orientation of the Néel vector in CrSb precludes the occurrence of anomalous Hall effect, [17–20] the non-linear behavior can be attributed to the multicarrier mechanism (see Supporting Information). [19, 21] Figure 3f presents the Hall coefficient, R_{ijk} , as a function of temperature for all Hall measurement geometries, evaluated at 0 T (low-field limit) and 9 T (high-field limit) using the equation: $R_{ijk}(B_0) = \left. \frac{d\rho_{ij}}{dB_k} \right|_{B_0}$. In a multicarrier system, the non-linear nature of Hall resistivity results in distinct low-field and high-field values for the Hall coefficient. The low-field value carries information of both carrier density and mobility, while the high-field value only carries the information of carrier density. [16, 22] Since both parameters play a crucial role in the overall conduction, the low-field value of the Hall coefficient is more reliable for determining the dominant conduction type in a material, with positive value indicating hole-dominant conduction and negative value indicating electron-dominant conduction. Across all temperatures, the low-field value of R_{zyx} and R_{xzy} remain positive, while that of R_{yxz} remains negative, inferring that the transport is dominated by electrons when the magnetic

field is applied along the c -axis and by holes when the magnetic field is applied in the ab -plane of the hexagonal CrSb crystal. The sign of R_{ijk} seems to be dictated only by the direction of the applied magnetic field, regardless of the direction of applied current. For two in-plane currents, $j||x$ and $j||y$, R_{yxz} and R_{zyx} have opposite signs, whereas for in-plane and out-of-plane currents, $j||y$ and $j||z$, R_{zyx} and R_{xzy} have the same sign. This happens because the trajectory of charge carrier (and hence the conduction direction) is determined by the direction of the magnetic field rather than the direction of the applied current in Hall effect measurements. In particular, the trajectory of charge carrier is given by the intersection of the FS by a plane perpendicular to the magnetic field as shown in Figure 1. [16, 22] The applied electric field (i.e; current) induces only a minute distortion in the FS and thus negligibly affects the trajectory of the charge carriers. Consequently, an in-plane magnetic field induces cross-plane conduction, whereas a cross-plane magnetic field induces in-plane conduction. This suggests that the in-plane conduction is electron-dominated whereas the cross-plane conduction is hole dominated. The identical sign and magnitude of R_{zyx} and R_{xzy} is a direct consequence of the magnetic point group ($6'/m'mm'$) symmetry of CrSb which imposes the constraint $R_{zyx} = R_{xzy}$. [19, 23]

An alternative and potentially more reliable tool for determining the polarity of charge carriers in a material is the thermopower experiment, as it does not involve the application of an external magnetic field. By applying a temperature gradient across the material and measuring the longitudinal voltage generated, the Seebeck coefficient (S_{ii}), which quantifies the voltage generated per unit temperature difference $S_{ii} = -\frac{\Delta V_i}{\Delta T_i}$, can

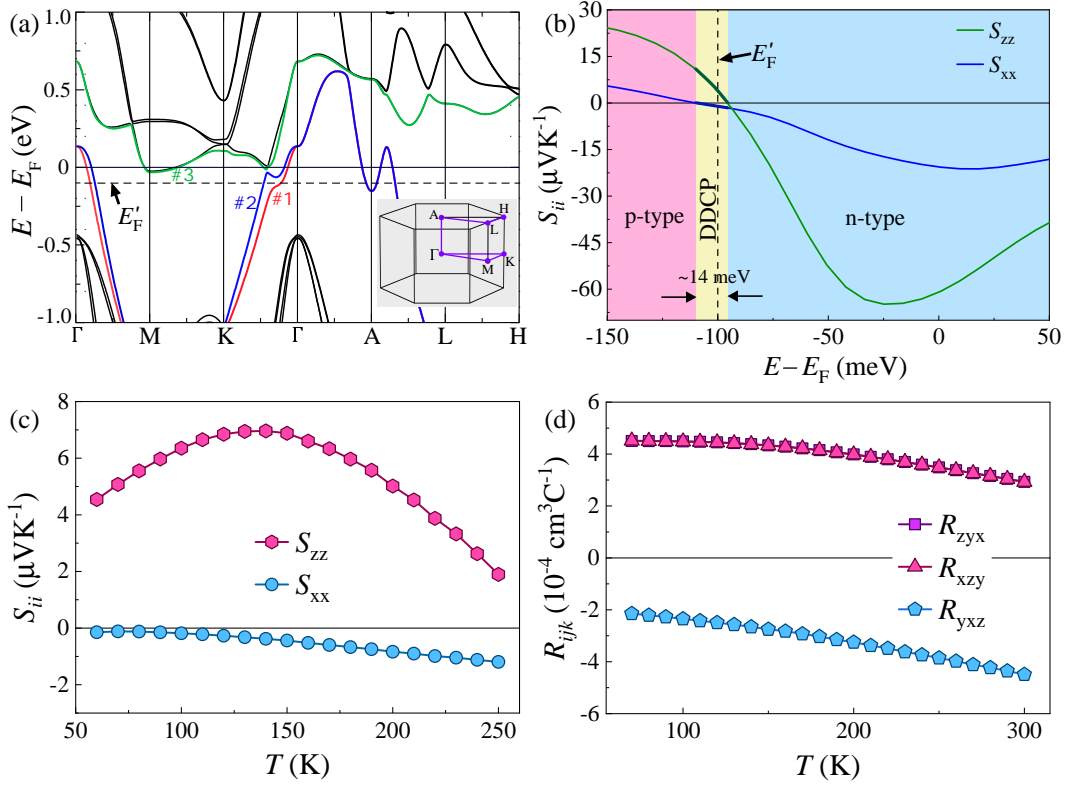


Figure 4. Results of theoretical calculations on CrSb. (a) Band structure along high-symmetry paths (see inset) of the BZ with SOC turned on. The bands crossing the shifted E'_F (dashed line) are highlighted in color and labeled numerically. (b) In-plane (S_{xx}) and cross-plane (S_{zz}) Seebeck coefficients at 100 K as a function of change in Fermi energy showing the DDCP behavior existing within a small energy window. The black dashed line represents the shifted Fermi energy E'_F (see text). (c) Temperature dependence of S_{xx} and S_{zz} calculated at E'_F . (d) Temperature dependence of the Hall coefficient components calculated at E'_F .

be defined. [24] Electrons and holes produce negative and positive Seebeck coefficients, respectively. Thus, by examining the sign of Seebeck coefficients measured along different crystallographic directions, the type of charge carrier dominating the conduction along those directions can be determined. Figure 3g shows the temperature dependence of both the in-plane (S_{xx}) and cross-plane (S_{zz}) Seebeck coefficients. In the measured temperature range, S_{xx} increases towards negative values, while S_{zz} increases towards positive values with temperature. Notably, S_{xx} remains negative while S_{zz} remains positive at all measured temperatures, indicating electron-dominant conduction in the plane and hole-dominant conduction across the plane of the hexagonal CrSb crystal. Although electrons and holes produce Seebeck coefficients with opposite signs, the opposite signs of the Seebeck coefficient can, in principle, arise from other direction-dependent terms in the following tensor expression of the Seebeck coefficient: [1, 6]

$$S_{ii} = -\frac{\pi^2 K_B^2 T}{3|e|} \left[\frac{1}{n(E)} \frac{dn(E)}{dE} + \frac{1}{\tau_{ii}(E)} \frac{d\tau_{ii}}{dE} + m_{ii}^* \frac{d}{dE} \left(\frac{1}{m_{ii}^*} \right) \right]_{E=E_F}. \quad (2)$$

Here, $n(E)$ and $\tau_{ii}(E)$ are the energy dependent carrier concentration and relaxation-time tensor. Although $n(E)$ is a scalar and cannot cause anisotropy in the sign of S_{ii} , $\tau_{ii}(E)$ is a tensor and can have different values in

different directions. However, the quantity $\frac{1}{\tau_{ii}(E)} \frac{d\tau_{ii}}{dE}$, which appears in the expression of S_{ii} , depends on the nature of the scattering mechanism of the conduction electrons and must have an isotropic sign in a clean single crystal having negligible defects. The isotropy of scattering processes in CrSb is also evidenced by the isotropic values of in-plane and cross-plane longitudinal resistivity. Thus, the anisotropy in the sign of S_{ii} must arise from m_{ii}^* as the quantity $\frac{d}{dE} \left(\frac{1}{m_{ii}^*} \right)$ is always negative for energy bands with cosine-like dispersion. [1]

We investigated the microscopic origin of direction-dependent changes in the nature of charge carriers involved in the transport of CrSb within DFT calculations. Figure 4a shows the band structure of CrSb, plotted along high-symmetry paths of the BZ [see the inset of Figure 4a] with spin-orbit coupling turned on. Since all these paths lie within the spin-degenerate nodal planes, protected by the sublattice-transposing symmetry of the CrSb crystal (see Supporting Information), the bands along these paths do not experience altermagnetic spin-splitting. Real crystals often deviate from perfect stoichiometry, which changes the position of the Fermi energy. This must, however, be considered in the DFT calculations to capture the trends seen in the experiment. We find that adding a small number of holes per unit cell ($\sim 0.13/\text{u.c.}$) induces DDCP. In this case, the Fermi energy E_F is shifted below by 100 meV to E'_F , represented

by the black dashed line in Figs. 4(a) and 4(b). To understand the unusual experimental results, we theoretically calculated the thermopower and the Hall coefficient tensor within the DFT framework using the Boltzmann transport equations and the relaxation-time approximation. The calculated Seebeck coefficient at 100 K is plotted as a function of the change in chemical potential in Figure 4b. It shows that direction-dependent conduction polarity exists within a narrow energy window (~ 14 meV) around E'_F . The FS obtained at E'_F [see Figure 5] is in good agreement with the FS observed in ARPES studies on CrSb, [25–27] confirming that Fermi energy is indeed shifted below its theoretical value in this system.

The temperature-dependent in-plane (S_{xx}) and cross-plane (S_{zz}) Seebeck coefficients are presented in Figure 4c. Within the examined temperature range, the absolute value of S_{xx} exhibits a slight, monotonic increase with increasing temperature. Conversely, the absolute value of S_{zz} initially rises with temperature, reaches a broad peak, and then decreases. However, S_{xx} remains negative across this temperature range, while S_{zz} is positive, which is qualitatively consistent with the experimental observations. Figure 4d shows the computed Hall coefficient components as a function of temperature. While R_{yxx} remains negative throughout the chosen temperature range, R_{yzz} and R_{zyx} stay positive. The constraint $R_{yzz} = R_{zyx}$, dictated by the magnetic point group symmetry of CrSb, is also accurately reflected. The trends in Hall coefficients are also consistent with the experimental observations. These results suggest that the in-plane conduction is electron-dominated, while the cross-plane conduction is hole-dominated.

To understand the mechanism of DDCP in CrSb, we calculated the FS at E'_F , as shown in Figure 5a. Three distinct Fermi pockets labeled α , β , and γ correspond to three different bands (#1, #2, and #3, respectively) that cross E'_F . Although band #3 does not cross E'_F at $k_z = 0$ plane, it crosses E'_F at some finite value of k_z , as shown in Supporting Information Figure S7. The α and β pockets appear to be nearly hyperboloid in shape, meaning they are closed in the $k_x - k_y$ plane and open along the k_z direction, apparently exhibiting both convex and concave features. Each of these pockets includes a small hemispherical sub-pocket around A point of the BZ. The γ pocket consists of 12 symmetry-related similar sub-pockets. These sub-pockets are closed and have an anisotropic, bead-like shape, elongated along the k_z -direction.

In the presence of multiple Fermi pockets with varying geometries, including hyperboloid-like and anisotropic features, the mechanism of DDCP in CrSb may not be determined simply by observing the shape of the FS. We therefore investigated the origin of this behavior by calculating the inverse effective mass (IEM) tensor, m_{ij}^{*-1} , at each point of the FS. This involves the curvature of the electronic band dispersion at that point, as described by Eq. (1). Figure 5b-d shows the distribution of the diagonal components of the IEM tensor, normalized by the free electron mass (m_e), on the three Fermi pockets. The pockets α and β host both positive and negative distribution of IEM along both in-plane (x and y) and cross-plane (z) directions, with negative IEM appar-

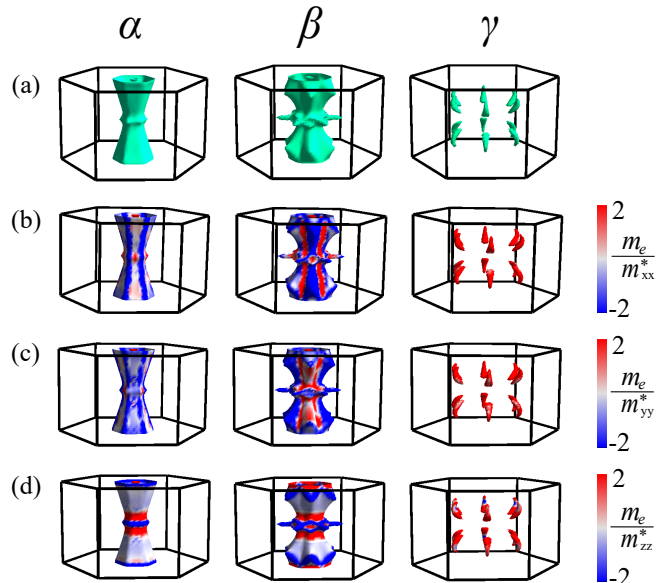


Figure 5. (a) Calculated Fermi pockets α , β , and γ associated with three distinct bands #1, #2, and #3, respectively, that cross E'_F . (b)-(d) The distribution of IEM strength on the Fermi pockets along (b) x-, (c) y-, and (d) z-directions.

ently dominating the overall distribution. In contrast, the pocket γ has predominantly positive IEM along all directions, indicating that it is an electron pocket. Notably, the small hemispherical α and β sub-pockets also display positive IEM along all directions, indicating that they are electron pockets as well. Table 1 presents the IEM values averaged over each of the three individual Fermi pockets and over the entire FS along x, y and z-directions. From this table, it is evident that both the α and β pockets do not produce DDCP on their own (goniopolarity) as they have an overall hole character (negative effective mass) along all the directions. The average IEM values for the γ pocket along all directions are positive which means it has overall electron character along all the directions. When the entire FS is considered, the in-plane average IEM values become positive, while the cross-plane average IEM value becomes negative, giving rise to DDCP. This suggests that DDCP in CrSb arises from the multicarrier mechanism, where in-plane conduction is dominated by electrons and cross-plane conduction is dominated by holes.

Our DFT calculations predict that DDCP exists only within a small energy range ($\Delta E \approx 14$ meV) around

Table 1: Average normalized inverse effective mass (IEM) values for the individual Fermi pockets α , β , γ and the entire FS along different directions.

	α	β	γ	FS
$\langle \frac{m_e}{m_{xx}^*} \rangle$	-1.65	-1.16	4.42	0.04
$\langle \frac{m_e}{m_{yy}^*} \rangle$	-1.63	-1.15	4.37	0.05
$\langle \frac{m_e}{m_{zz}^*} \rangle$	-0.47	-2.33	4.55	-1.56

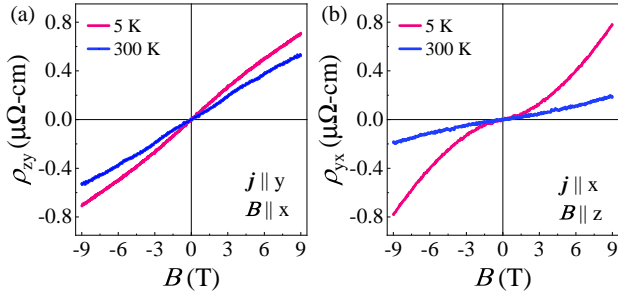


Figure 6. Magnetic field dependent Hall resistivity of $\text{Cr}_{0.98}\text{V}_{0.02}\text{Sb}$ at temperatures 5 K and 300 K for (a) in plane ($B \parallel x$) and (b) out-of-plane ($B \parallel z$) magnetic fields.

E'_F . To test the validity of this, we doped CrSb with 2% V and synthesized $\text{Cr}_{0.98}\text{V}_{0.02}\text{Sb}$. This introduces an additional 0.04 number of holes per unit cell which is expected to move the system out of the DDCP window. Figure 6a and 6b show the field-dependent Hall resistivity ρ_{zy} and ρ_{yx} , respectively for $\text{Cr}_{0.98}\text{V}_{0.02}\text{Sb}$ at temperatures 5 K and 300 K. While the hole doping has little effect on ρ_{zy} , as evidenced by its similar positive slopes for CrSb and $\text{Cr}_{0.98}\text{V}_{0.02}\text{Sb}$ (see 300 K data), it significantly modifies ρ_{yx} , which retains non-linearity but now exhibits positive slopes, indicating hole-dominant conduction. This confirms that even a small amount of hole doping suppresses the DDCP and renders the system p-type, consistent with our DFT predictions.

3 Conclusion

In summary, we have studied the anisotropic transport properties of altermagnetic CrSb. Both Hall and Seebeck coefficients indicate that CrSb exhibits DDCP, with in-plan conduction dominated by electrons and cross-plane conduction dominated by holes. Our DFT calculations based on the Boltzmann transport equation and the relaxation-time approximation qualitatively support our experimental results. We identify two hole pockets and one electron pocket dominating the cross-plane and in-plane conduction, respectively. Furthermore, our calculations predict that the DDCP in CrSb is fragile and can be suppressed with a small amount of doping. This prediction is validated by the loss of DDCP in minimally hole doped $\text{Cr}_{0.98}\text{V}_{0.02}\text{Sb}$. Composed of earth-abundant and non-toxic elements, CrSb emerges as a promising candidate for practical applications leveraging the DDCP behavior. Furthermore, the inherent altermagnetic nature of CrSb, characterized by large spin-splitting, opens up exciting possibilities for future spintronic applications that can exploit both DDCP and spin-splitting phenomena.

4 Method

Crystal growth and characterization: Single crystals of CrSb and $\text{Cr}_{0.98}\text{V}_{0.02}\text{Sb}$ were grown by the chemical vapor transport (CVT) method. To grow CrSb, Cr (99.99%, *Alfa Aesar*) and Sb powders (99.8%, *Alfa Aesar*) (1 g in total) were taken in a 1 : 1 molar ratio

together with 100 mg of iodine and sealed in a quartz tube 160 mm long and 15 mm in diameter. The tube was then evacuated, sealed under a partial Ar atmosphere, and placed in a horizontal three-zone tube furnace for 10 days. A uniform temperature gradient was maintained along the tube for the transport process, keeping the reactant end of the tube at 750 °C and the product end at 650 °C. Large hexagonal plate-like single crystals up to 1 mm thick and 5 mm wide were formed near the product end of the tube at the end of the reaction. Single crystals of $\text{Cr}_{0.98}\text{V}_{0.02}\text{Sb}$ were grown following the same process with the starting ratio of elements.

The elemental composition was verified using energy dispersive x-ray spectroscopy (EDXS) (see Supporting Information). The EDXS data were collected on a field emission electron microscope (Quanta 250 FEG) equipped with an Element silicon drift detector (SDD) with an accelerating voltage of 25 kV and an accumulation time of 60 seconds. X-ray diffraction (XRD) experiments were performed using a Rigaku SmartLab diffractometer equipped with a 9 kW Cu k_α X-ray source. The phase purity of CrSb was verified using powder X-ray diffraction, where the pattern was fitted using the Le-Bail method (see Supporting Information).

Electrical transport and thermopower experiments: The magnetotransport measurements were carried out using the ETO (electrical transport option) option of the Physical Properties Measurement System (PPMS, 9 T, Dynacool, Quantum Design). A standard six-terminal method was employed for simultaneous measurements of longitudinal resistivity (ρ_{ii}) and transverse Hall resistivity (ρ_{ij}). The indices i and j in ρ_{ij} are the direction of measured voltage and applied current, respectively. Proper symmetrisation and anti-symmetrisation were done to get rid of any additional contribution coming from possible misalignment of the contact probes.

The thermopower measurements were carried out on a bulk single crystal in both directions. The two probe electrodes were made on top of the crystal sample by fixing Cu-wires using silver paste. These measurements were done in a liquid nitrogen cryostat where the sample was kept under vacuum. The temperature difference between two ends of the sample was generated by sending currents from a source meter (Keithley 2450) to the heater attached just beside the sample. The voltage and temperature difference between two ends of the sample were measured by a precision nano voltmeter (Keithley 2182A) and temperature controller (Lakeshore 340). The bath temperature is controlled using a temperature controller (Lakeshore 340) with temperature fluctuations less than ± 20 mK.

DFT Calculations: The electronic structure was computed within the Vienna Ab initio Simulation Package (VASP), employing a plane-wave basis set and projected augmented wave potentials. [28–31] The generalized gradient approximation (GGA) [32] for the exchange-correlation functional was used. While the lattice parameters were fixed at the experimental values [33] for the NiAs structure of CrSb in the $P6_3/mmc$ spacegroup, all internal atomic positions were optimized through a total energy minimization. A cutoff energy of 500 eV was used to define the maximum kinetic energy for the

plane waves in the basis. Brillouin zone integrations were performed with a Monkhorst-Pack k -grid of density $10 \times 10 \times 10$ points. [34] The Seebeck and Hall coefficients were calculated using the semiclassical Boltzmann transport equation. These calculations employed the relaxation time and rigid band approximations, with the DFT band dispersions interpolated on a dense $35 \times 35 \times 35$ k -mesh grid as implemented in Boltztrap2. [35] Additionally, the inverse effective mass (IEM) tensor was determined using B-spline interpolation of the DFT band dispersions.

Acknowledgements

This work utilized the instrumentation facilities provided by the Technical Research Centre (TRC) at S. N. Bose National Centre for Basic Sciences, under Department of Science and Technology (DST), Government of India. NK acknowledges the Science and Engineering Research Board (SERB), India, for financial support through Grant Sanction No. CRG/2021/002747 and Max Planck Society for funding under Max Planck-India partner group project. PM acknowledges support from SERB through the project SERB-POWER (SPF/2021/000066). MM acknowledges CSIR-Human Resource Development Group (HRDG) (03/1511/23/EMR-II). BR acknowledges the financial support from DST.

Conflict of interest

The authors declare no conflict of interest.

References

- [1] Bin He, Yaxian Wang, Maxx Q. Arguilla, Nicholas D. Cultrara, Michael R. Scudder, Joshua E. Goldberger, Wolfgang Windl, and Joseph P. Heremans. The fermi surface geometrical origin of axis-dependent conduction polarity in layered materials. *Nat. Mater.*, 18:568–572, 2019.
- [2] Karl G. Koster, Ziling Deng, Curtis E. Moore, Joseph P. Heremans, Wolfgang Windl, and Joshua E. Goldberger. Axis-dependent conduction polarity in WSi_2 single crystals. *Chem. Mater.*, 35:4228–4234, 2023.
- [3] Naoto Nakamura, Yosuke Goto, and Yoshikazu Mizuguchi. Axis-dependent carrier polarity in polycrystalline NaSn_2As_2 . *Appl. Phys. Lett.*, 118(15):153903, 2021.
- [4] C. Helman, A. M. Llois, and M. Tortarolo. Ordinary Hall anomaly due to the fermi surface shape in MnAs . *Phys. Rev. B*, 104(19):195109, 2021.
- [5] Andrew M. Ochs, Prashun Gorai, Yaxian Wang, Michael R. Scudder, Karl Koster, Curtis E. Moore, Vladan Stevanovic, Joseph P. Heremans, Wolfgang Windl, Eric S. Toberer, and Joshua E. Goldberger. Computationally guided discovery of axis-dependent conduction polarity in NaSnAs crystals. *Chem. Mater.*, 33:946–951, 2021.
- [6] Yaxian Wang, Karl G. Koster, Andrew M. Ochs, Michael R. Scudder, Joseph P. Heremans, Wolfgang Windl, and Joshua E. Goldberger. The chemical design principles for axis-dependent conduction polarity. *J. Am. Chem. Soc.*, 142:2812–2822, 2020.
- [7] Siyun Qi, Jian Liu, Yangyang Li, and Mingwen Zhao. Tunable goniopolarity of graphenelike boron layers in metal diborides. *Phys. Rev. B*, 106(16):165204, 2022.
- [8] Yang Tang, Boya Cui, Chuanle Zhou, and Matthew Grayson. $p \times n$ -type transverse thermoelectrics: A novel type of thermal management material. *J. Electron. Mater.*, 44:2095–2104, 2015.
- [9] Hikari Manako, Shoya Ohsumi, Yoshiki J Sato, R Okazaki, and D Aoki. Large transverse thermoelectric effect induced by the mixed-dimensionality of fermi surfaces. *Nat. Commun.*, 15(1):3907, 2024.
- [10] Michael R. Scudder, Bin He, Yaxian Wang, Akash Rai, David G. Cahill, Wolfgang Windl, Joseph P. Heremans, and Joshua E. Goldberger. Highly efficient transverse thermoelectric devices with Re_4Si_7 crystals. *Energy Environ. Sci.*, 14(7):4009–4017, 2021.
- [11] Libor Šmejkal, Jairo Sinova, and Tomas Jungwirth. Beyond conventional ferromagnetism and antiferromagnetism: A phase with nonrelativistic spin and crystal rotation symmetry. *Phys. Rev. X*, 12(3):031042, 2022.
- [12] Libor Šmejkal, Jairo Sinova, and Tomas Jungwirth. Emerging research landscape of altermagnetism. *Phys. Rev. X*, 12(4):040501, 2022.
- [13] A. I. Snow. Neutron diffraction investigation of the atomic magnetic moment orientation in the antiferromagnetic compound CrSb . *Phys. Rev.*, 85(2):365–365, 1952.
- [14] Jibao Yuan, Yuzhu Song, Xianran Xing, and Jun Chen. Magnetic structure and uniaxial negative thermal expansion in antiferromagnetic CrSb . *Dalton Trans.*, 49:17605–17611, 2020.
- [15] Naoto Nagaosa, Jairo Sinova, Shigeki Onoda, A. H. MacDonald, and N. P. Ong. Anomalous Hall effect. *Rev. Mod. Phys.*, 82(2):1539–1592, 2010.
- [16] Colin Hurd. *The Hall effect in metals and alloys*. Springer Science & Business Media, 2012.
- [17] Andriy Smolyanyuk, Libor Šmejkal, and Igor I Mazin. A tool to check whether a symmetry-compensated collinear magnetic material is antiferro- or altermagnetic. *SciPost Physics Codebases*, page 030, 2024.

- [18] Zhiyuan Zhou, Xingkai Cheng, Mengli Hu, Junwei Liu, Feng Pan, and Cheng Song. Crystal design of altermagnetism. *arXiv preprint arXiv:2403.07396*, 2024.
- [19] Takahiro Urata, Wataru Hattori, and Hiroshi Ikuta. High mobility charge transport in a multicarrier altermagnet CrSb. *Phys. Rev. Mater.*, 8(8):084412, 2024.
- [20] Tianye Yu, Ijaz Shahid, Peitao Liu, Xing-Qiu Chen, and Yan Sun. Néel vector-dependent anomalous transport in altermagnetic metal CrSb. *arXiv preprint arXiv:2412.12882*, 2024.
- [21] Yuqing Bai, Xinji Xiang, Shuang Pan, Shichao Zhang, Haifeng Chen, Xi Chen, Zhida Han, Guizhou Xu, and Feng Xu. Nonlinear field dependence of Hall effect and high-mobility multi-carrier transport in an altermagnet CrSb. *arXiv preprint arXiv:2409.14855*, 2024.
- [22] Neil W Ashcroft, N David Mermin, and Sergio Rodriguez. Solid state physics. *American Journal of Physics*, 46(1):116–117, 1978.
- [23] R.R. Birss. *Symmetry and Magnetism*. Selected topics in solid state physics. North-Holland Publishing Company, 1964.
- [24] Kamran Behnia. *Fundamentals of thermoelectricity*. OUP Oxford, 2015.
- [25] Jianyang Ding, Zhicheng Jiang, Xiuhua Chen, Zicheng Tao, Zhengtai Liu, Tongrui Li, Jishan Liu, Jianping Sun, Jinguang Cheng, Jiayu Liu, Yichen Yang, Runfeng Zhang, Liwei Deng, Wenchuan Jing, Yu Huang, Yuming Shi, Mao Ye, Shan Qiao, Yilin Wang, Yanfeng Guo, Donglai Feng, and Dawei Shen. Large band splitting in g-wave altermagnet CrSb. *Phys. Rev. Lett.*, 133(20):206401, 2024.
- [26] Meng Zeng, Ming-Yuan Zhu, Yu-Peng Zhu, Xiang-Rui Liu, Xiao-Ming Ma, Yu-Jie Hao, Pengfei Liu, Gexing Qu, Yichen Yang, Zhicheng Jiang, Kohei Yamagami, Masashi Arita, Xiaoqian Zhang, Tian-Hao Shao, Yue Dai, Kenya Shimada, Zhengtai Liu, Mao Ye, Yaobo Huang, Qihang Liu, and Chang Liu. Observation of spin splitting in room-temperature metallic antiferromagnet CrSb. *Adv. Sci.*, 11(43):2406529, 2024.
- [27] Guowei Yang, Zhanghuan Li, Sai Yang, Jiyuan Li, Hao Zheng, Weifan Zhu, Saizheng Cao, Wenxuan Zhao, Jiawen Zhang, Mao Ye, Yu Song, Lun-Hui Hu, Lexian Yang, Ming Shi, Huiqiu Yuan, Yongjun Zhang, Yuanfeng Xu, and Yang Liu. Three-dimensional mapping and electronic origin of large altermagnetic splitting near fermi level in CrSb. *arXiv preprint arXiv:2405.12575*, 2024.
- [28] P. E. Blöchl. Projector augmented-wave method. *Phys. Rev. B*, 50:17953–17979, 1994.
- [29] G. Kresse and J. Hafner. Ab initio molecular dynamics for liquid metals. *Phys. Rev. B*, 47:558–561, 1993.
- [30] G. Kresse and J. Hafner. Ab initio molecular-dynamics simulation of the liquid-metal-amorphous-semiconductor transition in germanium. *Phys. Rev. B*, 49:14251–14269, 1994.
- [31] G. Kresse and J. Furthmüller. Efficient iterative schemes for ab initio total-energy calculations using a plane-wave basis set. *Phys. Rev. B*, 54:11169–11186, 1996.
- [32] John P. Perdew, Kieron Burke, and Matthias Ernzerhof. Generalized gradient approximation made simple. *Phys. Rev. Lett.*, 77:3865–3868, 1996.
- [33] A. Kallel, H. Boller, and E.F. Bertaut. Helimagnetism in MnP-type compounds: MnP, FeP, CrAs and CrAs_{1-x}Sb_x mixed crystals. *J. Phys. Chem. Solids*, 35(9):1139–1152, 1974.
- [34] Hendrik J. Monkhorst and James D. Pack. Special points for Brillouin-zone integrations. *Phys. Rev. B*, 13:5188–5192, 1976.
- [35] Georg K.H. Madsen, Jesús Carrete, and Matthieu J. Verstraete. BoltzTraP2, a program for interpolating band structures and calculating semi-classical transport coefficients. *Comput. Phys. Commun.*, 231:140–145, 2018.